Supporting Information

Jensen et al. 10.1073/pnas.0911691107

SI Text

Materials and Methods. ***System preparation.*** We embedded the pore domain (S4-S5 linker helix and helices S5 and S6; residues 312–421) of Kv1.2 [Protein Data Bank (PDB) entries 2A79 and 2R9R (1, 2)] into a palmitoyl oleolyl phosphatidyl ethanolamine (POPE) lipid bilayer solvated in 0.6 M KCl. All protein residues were modeled according to their titration state at neutral pH, leaving the protein with a net charge of $-8e$. The total number of atoms was approximately 70,000: 98 K^+ and 90 Cl^- ions, about 10,000 water molecules, and 271 POPE molecules. The system measured roughly $98 \times 98 \times 83$ Å^3. We initially configured the occupancy of the pore with three K^+ ions at selectivity filter (SF) sites S6, S3, and S1 and two water molecules at sites S2 and S4.

Simulations. Depolarizing and hyperpolarizing transmembrane potentials (-180 mV $< V <$ $+180$ mV) were imposed as constant electric fields, E, along the pore axis, z. To obtain the applied voltage, V, from E, we assumed that the entire potential drop occurs across the SF (3, 4); this implies $V = E\Delta z$, where $\Delta z = 13.4 \pm 0.2$ Å is the distance between Thr374:O_γ and Tyr377:O, averaged over all simulations at depolarizing voltages. Thirty-one simulations were performed with an aggregate length of more than ~30 μs (summarized in Table S1). All simulations were performed using Desmond (5) at constant pressure and temperature (NPT ensemble; 310 K, 1 bar) and Berendsen coupling scheme (6) with one temperature group. All bond lengths to hydrogen atoms were constrained using M-SHAKE (7). Van der Waals and short-range electrostatic interactions were cut off at 10 Å. Long-range electrostatic interactions were computed by the particle mesh Ewald (PME) method (8) using a $64 \times 64 \times 64$ grid with $\sigma = 2.35$ Å and fifth-order B splines for interpolation. A time-reversible reference system propagator algorithm (RESPA) integrator (9) was used with a time step of 2 fs; long-range electrostatics were computed every 6 fs. In each simulation, the electric field was linearly increased to its final value over 9 ns, and initial harmonic positional restraints (24 kcal mol^{-1} Å^{-2}) on the protein were tapered off linearly over 27 ns.

Analysis. Coordinates were saved every 12 ps and were analyzed using HiMach (10); some analysis modules used Visual Molecular Dynamics (VMD) (11) for structure processing. Unless otherwise indicated, the initial 30 ns of all simulations were discarded as equilibration time.

Permeation through the Kv1.2 pore was recorded by tracking the positions of ions and water molecules as they passed through a region starting at Thr374:O_γ on the intracellular side and ending at Tyr377:O on the extracellular side, with a 2 Å buffer included on both sides. Only ions and water molecules that fully permeated this region were considered as contributing to a permeation event; complete permeation events are summarized in Table S1, and only these events contributed to the calculated kinetic occupancy histograms (Fig. 2*C* and Fig. S2*B*). Ion and water molecule currents were determined from the inverse mean waiting time between two consecutive permeation events; errors in the individual currents were determined by blocking analysis (12), while propagation of these errors was used to estimate errors in the H_2O/K^+ transport ratio (Fig. 1*D*).

We represented the three-ion configuration as a two-dimensional potential of mean force, using an in-house parallel implementation of the mixture-model fitting procedure described in Maragakis et al. (13) [see also Bowers et al. (14) and Baggenstoss (15)], with the maximum likelihood out of 10,000 attempts (Fig. 2*D*, 15 Gaussians; Fig. S3, 16 Gaussians).

Potassium occupancy across the pore (Fig. 4*A*) was calculated by constructing histograms of the ion positions for ions below the intracellular-facing side of the SF (Thr374:O_γ) and above the center of mass of Pro407 of the Pro405-Val406-Pro407 (PVP) constriction.

Water density across the pore (Fig. 4*B*) was calculated by building appropriately time-sliced histograms of water molecules found within a cylinder of 6 Å radius centered on the pore axis. Water occupancy in the cavity (Fig. 4*F*) was determined by counting the number of water molecules that resided below the intracellular-facing side of the SF (Thr374:O_γ) and above the center of mass of Pro407 of the PVP constriction. A median filter of 12-ns width was applied to the resulting occupancies.

Electron density within the SF and cavity (Fig. S2) was calculated using a five Gaussian approximation (16) on a 0.2-Å grid (1 Å^2 artificial temperature factor; Gaussians calculated within 3 Å of each atom position). Separate maps were calculated for K^+ ions, water molecules, and all other atoms. For comparison with crystallographic data, the K^+ and water maps were added to represent the observable X-ray density within the SF. Maps calculated from simulations under different biasing voltages were comparable to each other.

To allow for unbiased comparison of simulation and crystallographic maps, simulation maps were transformed to the same grid and coordinate frames used in the Kv1.2/Kv2.1 chimera (2) and KcsA (17) crystal structures. To account for Fourier series truncation and other experimental errors, only the experimentally observed structure factor indices were used, thereby replicating the observed data resolution limits and (in)completeness. To introduce experimental-like noise, the molecular dynamics (MD) structure factor amplitudes were randomly sampled from a Gaussian distribution (mean, original MD amplitude; SD, scaled crystallographic SD; negative randomized amplitudes reset to zero), and phases were randomly sampled from a phase-shifted (most-probable phase equal to original MD phase) unimodal phase distribution calculated using the crystallographic Hendrickson–Lattman coefficients. Centric reflection phases were shifted, after randomization, to the nearest of 0° or 180°. Overall, this procedure gave maps that were essentially indistinguishable from the original maps without added noise.

Kv1.2/2.1 chimera. A control simulation of the intact Kv1.2/Kv2.1 chimeric protein (2), comprising voltage sensing, pore, and T1 domains embedded into a POPE bilayer and solvated in 0.6 M KCl, was performed at 0 mV for ~1.7 μs. The total number of atoms was approximately 317,000: 816 K^+ and 820 Cl^- ions, about 77,000 water molecules, and 471 POPE molecules. The lipid-embedded chimeric channel measured initially roughly $150 \times 150 \times 150$ Å^3; thus, we used a $128 \times 128 \times 128$ Å^3 grid and $\sigma = 2.23$ Å in the PME electrostatics calculation. Pressure (1 bar) and temperature (310 K) were kept constant using the Martyna–Tobias–Klein method (18). All other aspects of the simulation protocol, in particular, the initial configuration of K^+ ions and H_2O molecules in the SF, were performed as in the pore-only simulations.

Visualization. Molecular images in the main text were rendered using PyMol (19). Molecular images were rendered using PyMol, POV-Ray (http://www.povray.org), and VMD (11).

1. Long SB, Campbell EB, MacKinnon R (2005) Crystal structure of a mammalian voltage-dependent Shaker family K^+ channel. *Science*, 309:897–903.
2. Long SB, Tao X, Campbell EB, MacKinnon R (2007) Atomic structure of a voltage-dependent K^+ channel in a lipid membrane-like environment. *Nature*, 450:376–382.
3. Berneche S, Roux B (2003) A microscopic view of ion conduction through the K^+ channel. *Proc Natl Acad Sci USA*, 100:8644–8648.
4. Neyton J, Miller C (1988) Potassium blocks barium permeation through a calcium-activated potassium channel. *J Gen Physiol*, 92:549–567.
5. Bowers KJ, et al. (2006) Scalable algorithms for molecular dynamics simulations on commodity clusters. *Proceedings of the ACM/IEEE Conference on Supercomputing (SC06)* (ACM Press, New York).
6. Berendsen HJC, Postma JPM, DiNola A, Haak JR (1984) Molecular dynamics with coupling to an external bath. *J Chem Phys*, 81:3684–3690.
7. Krautler V, van Gunsteren WF, Hunenberger PH (2001) A fast SHAKE algorithm to solve distance constraint equations for small molecules in molecular dynamics simulations. *J Comput Chem*, 22:501–508.
8. Darden T, York D, Pedersen L (1993) Particle mesh Ewald: an $N\cdot\log(N)$ method for Ewald sums in large systems. *J Chem Phys*, 98:10089–10092.
9. Tuckerman M, Berne BJ, Martyna GJ (1992) Reversible multiple time scale molecular dynamics. *J Chem Phys*, 97:1990–2001.
10. Tu T, et al. (2008) A scalable parallel framework for analyzing terascale molecular dynamics simulation trajectories. *Proceedings of the ACM/IEEE Conference on Supercomputing (SC08)* (ACM Press, New York).
11. Humphrey W, Dalke A, Schulten K (1996) VMD—visual molecular dynamics. *J Mol Graphics*, 14:33–38.
12. Flyvbjerg H, Petersen HG (1989) Error estimates on averages of correlated data. *J Chem Phys*, 91:461–466.
13. Maragakis P, van der Vaart A, Karplus M (2009) Gaussian-mixture umbrella sampling. *J Phys Chem B*, 113:4664–4673.
14. Bowers KJ, Devolder BG, Yin L, Kwan TJT (2004) A maximum likelihood method for linking particle-in-cell and Monte-Carlo transport simulations. *Comput Phys Commun*, 164:311–317.
15. Baggenstoss PM (2002) Statistical modeling using Gaussian mixtures and HMMs with Matlab. Tech Rep TM 03-128, Naval Undersea Warfare Center, Newport, RI.
16. Agarwal RC (1978) A new least-squares refinement technique based on the fast Fourier transform algorithm. *Acta Crystallogr*, A34:791–809.
17. Zhou Y, Morais-Cabral JH, Kaufman A, MacKinnon R (2001) Chemistry of ion coordination and hydration revealed by a K^+ channel-Fab complex at 2.0 Å resolution. *Nature*, 414:43–48.
18. Martyna GJ, Tobias DJ, Klein ML (1994) Constant pressure molecular dynamics algorithms. *J Comput Phys*, 101:4177–4189.
19. DeLano WL (2002) The PyMOL molecular graphics system (DeLano Scientific, San Carlos, CA). http://www.pymol.org.

Table S1. Summary of simulations

Voltage, mV	Time, ns	Final conformation	Permeation events K^+	Permeation events H_2O
		2A79		
+145	634.968	Open	45	49
+145	500.064	Open	63	52
+134	436.668	Inactivated	3	2
+134	612.672	Open	29	29
+123	884.388	Open	93	80
+116	164.276	Inactivated	2	2
+114	561.960	Inactivated	23	19
+112	1,015.308	Inactivated	22	18
+112	623.028	Open	18	18
+102	1,005.912	Open	40	38
+87	1,057.22	Closed	0	0
+87	1,090.824	Inactivated	16	14
+72	1,011.384	Open	8	9
+51	1,114.5844	Inactivated	2	4
Total	**10,713.260**		**364**	**334**
		Model		
0	1,176.158	Closed (symmetric)	0	0
+87	412.788	Closed (symmetric)	0	0
Total	**1,588.946**		0	0
		2R9R		
+178	276.299	Open	19	20
+156	408.924	Open	28	26
+134	534.406	Open	37	32
+123	752.424	Inactivated	25	21
+112	605.724	Open	38	38
+101	1,246.632	Open	28	21
+87	801.048	Open	15	15
+51	1,568.400	Inactivated	0	0
+26	2,085.144	Open	0	0
0	2,098.800	Closed	0	0
Subtotal	**10,377.801**		**190**	**173**
−26	2,000.400	Open	0	0
−51	2,000.400	Closed	1	0
−87	2,000.400	Closed	7	7
−123	2,000.400	Closed	9	10
−178	2,000.400	Closed	7	3
Subtotal	**10,002.000**		**24**	**20**
Total	**20,379.801**		**214**	**193**
		Intact 2R9R		
0	1,683.600	Open	0	0
Overall total	**34,365.607**		**578**	**527**

Applied voltage, simulation time, final conformation of the pore domain, and number of permeation events for K^+ ions and water molecules are listed for each simulation. Table is organized to reflect the fact that initial structures were based on PDB entries 2A79 (1) and 2R9R (2). Simulation time and permeation events are totaled for each initial structure and for all simulations combined. In eight simulations at depolarizing voltages (+51 to +134 mV), the channel underwent a conformational transition into an inactivated state that irreversibly attenuated the ionic current on the microsecond scale (Fig. S1). In most of these simulations, the pore domain steadily transported ions before current attenuation; permeation was analyzed up to that point. Occasionally, in simulations at large depolarizing voltages ($\geq +123$ mV), water molecules entered the outside of the selectivity filter, causing its distortion toward the end of the simulations (approximately the final 10% of simulation time given above). Permeation events were counted only up to that point. From the final closed (partially dewetted) conformation obtained at +87 mV (2A79), we constructed a 4-fold symmetric model ("Model") of the closed pore. During simulation (0 mV) this model remained closed but its subunits relaxed into an approximate two-by-two packing closely resembling the predominant pore conformation that resulted from simulations at hyperpolarizing, pore-closing voltages (Fig. 4). Subjecting the two-by-two packed conformation to a depolarizing voltage (+87 mV) did not result in pore opening over ~400 ns.

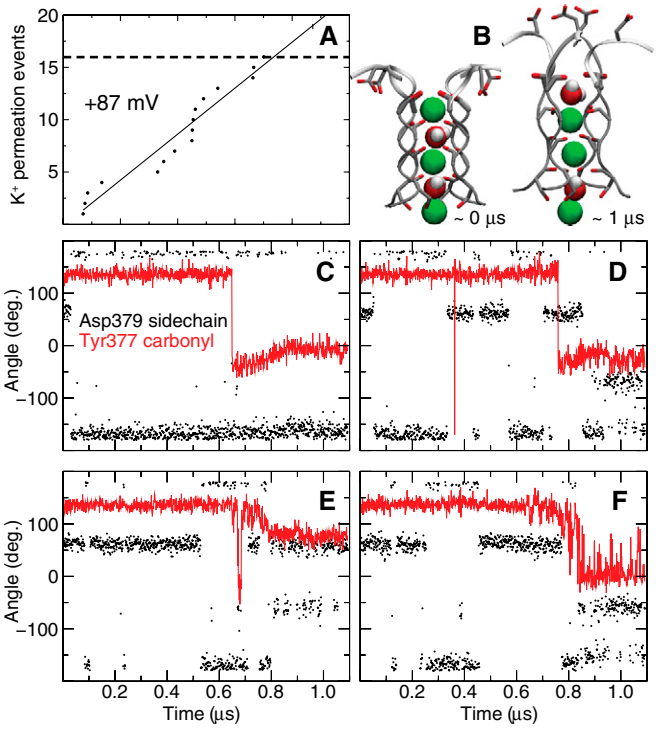

Fig. S1. Selectivity filter conformational change possibly related to (C-type) inactivation. (*A*) Ion permeation events vs. simulation time at a depolarizing voltage (+87 mV); permeation attenuated after ~0.7 μs, when the SF underwent a transition into a nonconductive state, as shown in *B*. (*B*) SF conformation in the conductive (*Left*, $t = 0$ μs) and nonconductive (*Right*, $t > \sim 0.7$ μs) states. The conformational change involved rotation of the Asp379 side chain (χ_1 torsion angle, N-C_α-C_β-C_γ), causing the side chain carboxylate to become exposed to the extracellular side, and rotation of the carbonyl groups of the four Tyr377 residues (ϕ torsion angle, N-C_α-C-O), causing these groups not to point toward the center of the SF lumen (the conductive conformation) but instead to align in a staggered, head-to-tail, low-energy arrangement. The Tyr377 conformational change was coupled to rotation of the ϕ angles of Gly376 and Gly378. In this nonconductive state, two K^+ ions were irreversibly (on the simulation timescale) trapped in SF sites S2 and S3; two water molecules located in S0 and S4 capped these ions. (*C–F*) Asp379 χ_1 (*Black*) and Tyr377 ϕ (*Red*) torsion angles vs. simulation time in each of the four subunits. The timescale of these conformational changes varied from ~100 to several hundred nanoseconds. Although these conformational changes typically occurred only hundreds of nanoseconds into a simulation, they may be related to experimentally observed C-type (extracellular) inactivation, albeit such inactivation is known to occur much more slowly, over $\sim 10^{-2} - 10^{1}$ s, and may involve larger conformational changes.

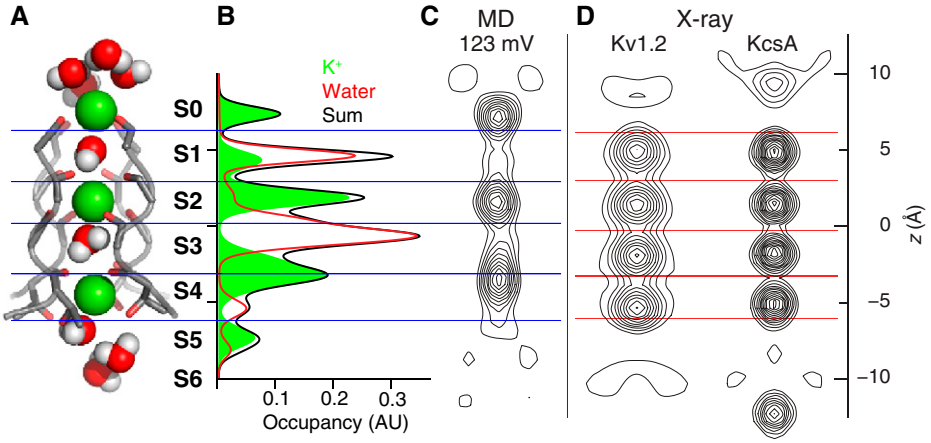

Fig. S2. Electron density within the selectivity filter. (*A*) Snapshot of the SF. (*B*) Occupancy across the SF computed from an MD trajectory (+123 mV), decomposed into contributions from K^+ ions and water molecules; AU, arbitrary units. (*C*) Electron density across the SF computed from an MD trajectory (+123 mV). (*D*) Experimental crystallographic electron density of Kv1.2 (2R9R) (2) and KcsA (1K4C) (17). In *C* and *D*, plots are contoured starting at 1.5σ above the map mean in 1.5σ steps. In *A–C*, blue lines delineate the average (over the four subunits) position of the carbonyl oxygen atoms (four upper lines) and the hydroxyl oxygen atom of Thr374 (lowest line) in the SF; red lines in *D* mark the corresponding positions in the Kv1.2 X-ray structure. The computationally determined electron density in *C* deviates from those observed experimentally in *D*. In addition to the possibility of force field artifacts, this difference may reflect that, in our simulations, the pore is in a conducting state and at a different temperature (310 K) than in the X-ray experiments (100 K).

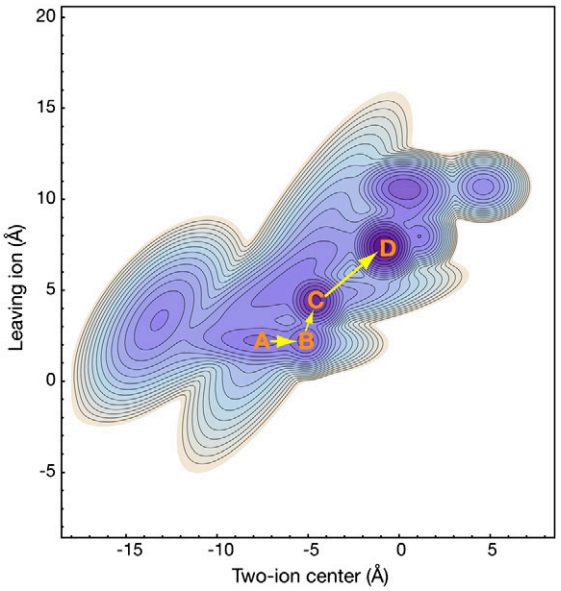

Fig. S3. Two-dimensional potential of mean force (PMF). Vertical and horizontal axes represent, respectively, the position (*z* coordinate) of an ion leaving the SF and the mean position of the two ions below it. From the PMF minima, we identified four three-ion configurations, or states, central to ion conduction, denoted A–D (as in the main text); arrows indicate transitions between these states. In cases of four-ion SF occupancy (see Fig. 2*B*), the three SF ions with the highest *z* coordinate were selected. We constructed each PMF from a fit to a Gaussian-mixture model of the samples (Fig. 2*B*) from our simulations.

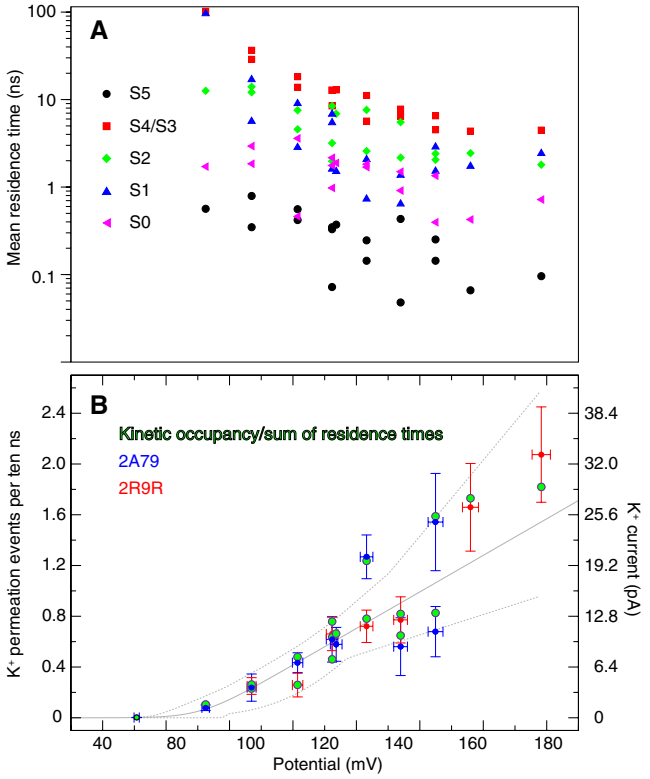

Fig. S4. Single-ion residence times. (*A*) Single-ion residence times (τ_r) in SF sites S0–S5. The S5 residence time was measured only for "productive" ions, i.e., those bound at S5 that did not subsequently dissociate back into the cavity. This time is short (note logarithmic scale) indicating that once a productive knock-on intermediate B (S5,[S4,S2]) (see Fig. 2*B* and Fig. S3) is formed, the transitions B → C(S5,[S3,S1]) → D(S4,[S2,S0]) follow rapidly; although they are voltage dependent, these steps are too fast to account for the overall voltage dependence of conduction. The S0 residence time is essentially constant, implying that dissociation from S0 to the extracellular side is largely voltage independent; it is also fairly fast. The slowest step, and the main source of voltage dependency, is thus formation of the knock-on intermediate B. (*B*) I_K–V relationship (see Fig. 1*C*) reconstructed from residence times (at each V, $I_K = O_K / \sum_i \tau_{r,i}$; $O_K = 2.4 \pm 0.1$, see main text and Fig. 2).

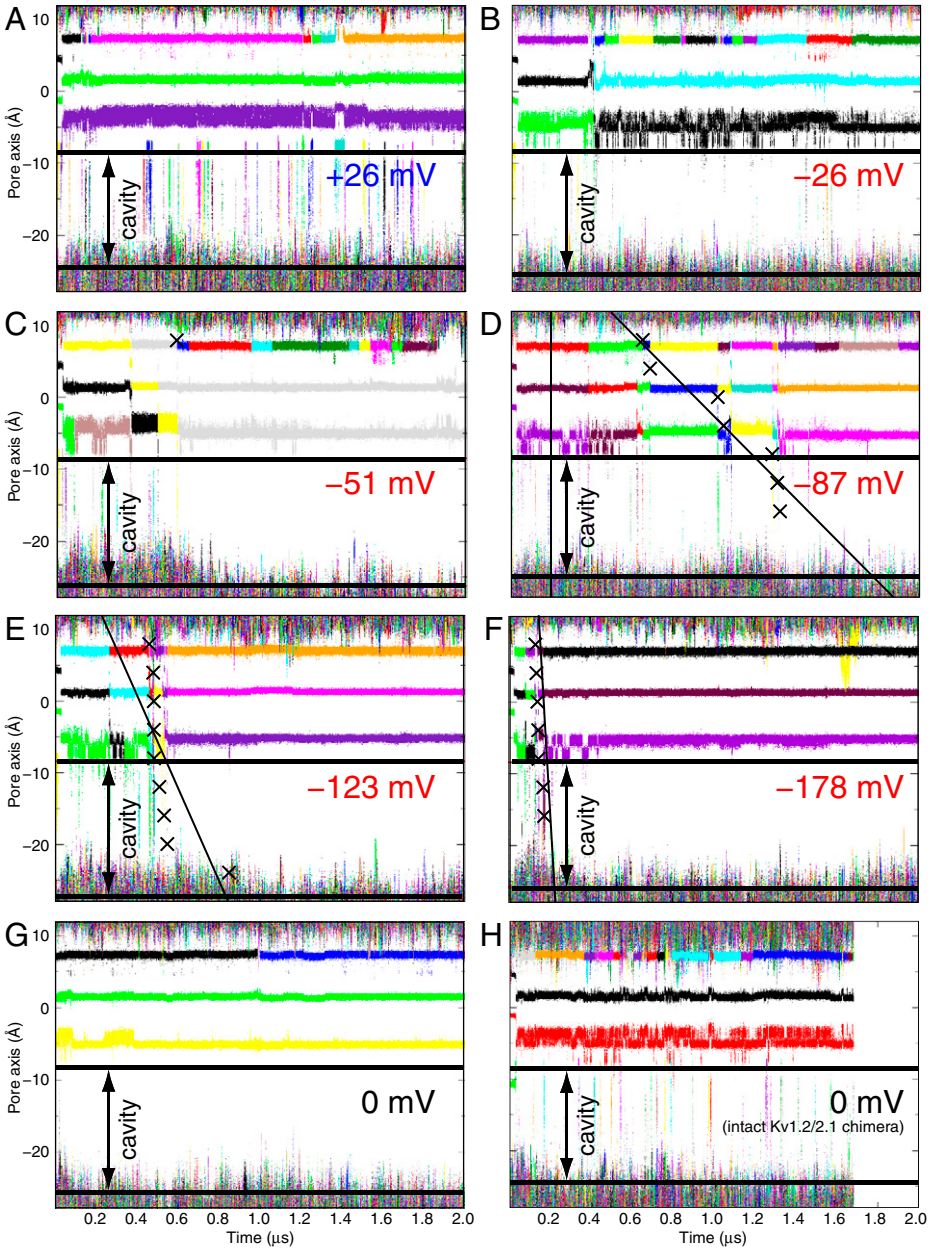

Fig. S5. Ion positions at small (thermal) voltages and hyperpolarizing voltages. Ion positions as function of time at thermal (*A*, *B*) and hyperpolarizing (*C*–*F*) voltages. At a depolarizing thermal voltage [$V = +26$ mV $\sim +k_BT/e$, (*A*)] the pore remains open and nonconducting, and the pore cavity is steadily occupied by K^+ ions. In contrast, at a hyperpolarizing thermal voltage [$V = -26$ mV $\sim -k_BT/e$, (*B*)], although the pore also remains open and nonconducting, the cavity is largely depleted of K^+ ions (see Fig. 4*A*). At larger hyperpolarizing voltages (*C*–*F*), the cavity undergoes closure after a short period of inward conduction (black crosses mark times of ion permeation events). At 0 mV, no conduction occurred and the pore closed after approximately 100 ns (*G*), whereas the intact channel, with voltage sensors retained, remained open for the entire simulation (1.7 μs) (*H*).

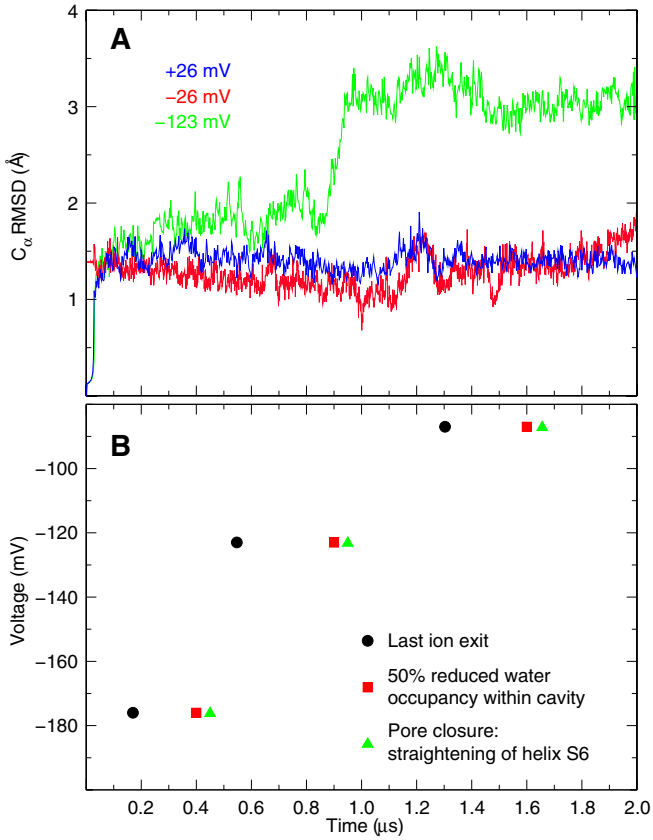

Fig. S6. Rms deviations and timing of key events at thermal voltages and hyperpolarizing voltages. (*A*) Rms deviations of C_α atoms at thermal voltages ($V = \pm 26$ mV), and at a large hyperpolarizing voltage (−123 mV) where the pore undergoes closure. (*B*) Sequence of key events that occurs during complete pore closure, as observed at the three most negative hyperpolarizing voltages. Notably, the delay between the exit time of the last ion and the time at which the cavity water occupancy is reduced by 50% is nearly constant. This constant and rather long delay of 200–300 ns suggests that electroosmotic water efflux at hyperpolarizing voltages is unlikely to be the root cause of cavity dewetting. Thus, the rate of dewetting is dictated by the similar density fluctuations at these three voltages, reflecting the essentially constant size of the hydrophobic confinement prior to its collapse.

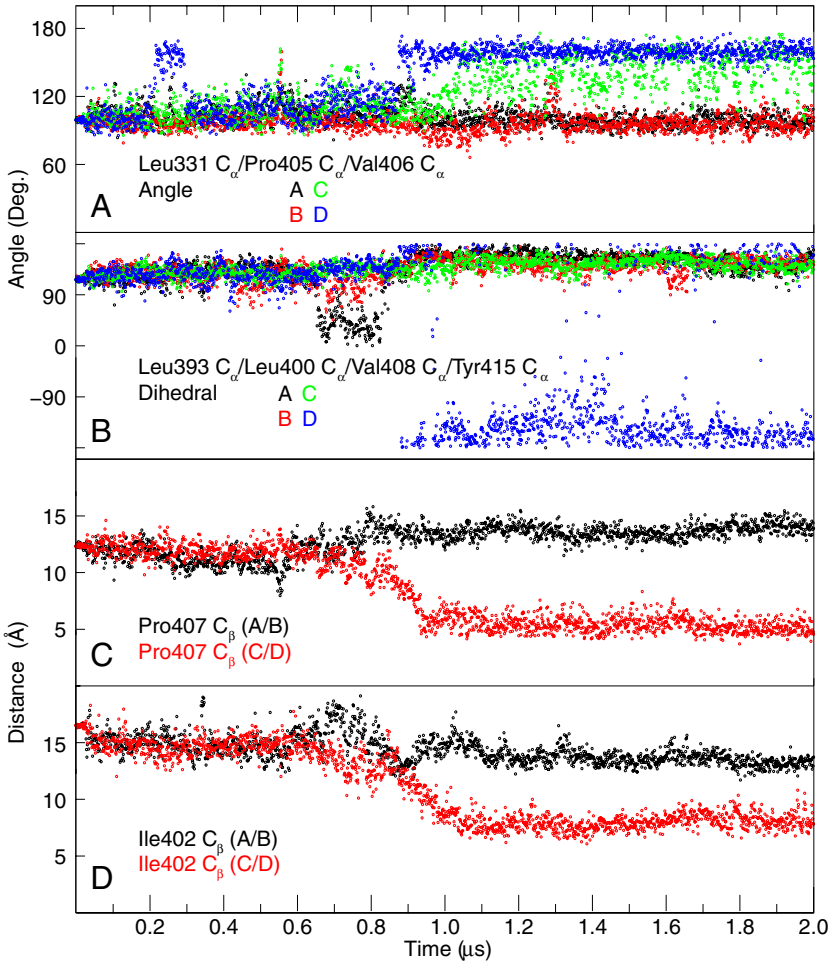

Fig. S7. Structural changes during pore closure. Structural changes observed during complete pore closure at a representative hyperpolarizing voltage (−123 mV). (*A*) Leu331/Pro405 side chain interchange: the angles between the Leu331 C_α/Pro405 C_α/Val406 C_α atoms of each subunit are shown. Note the interchange in subunit D (*Blue*) at about 0.9 μs. (*B*) Helix S6 straightening: the Leu393 C_α/Leu400 C_α/Val408 C_α/Tyr415 C_α dihedral angles are shown. S6 straightens in subunit D at about 0.9 μs. (*C*) Lower pore cavity constriction; the Pro407 C_α/Pro407 C_α distances, between subunits A and B (*Black*) and C and D (*Red*) across the Kv1.2 tetrameric pore domain diagonal, are shown. Note the gradual closure of subunits C and D beginning at about 0.7 μs. (*D*) Upper pore cavity constriction; the diagonal Ile402 C_α/Ile402 C_α distances are shown.

Fig. S8 (PDF)

Fig. S8. Pore cavity of diverse ion channels is hydrophobic. Primary sequences of several ion channels of diverse structure are aligned. Sequence alignments begin at the selectivity filter and continue through the approximate end of helix S6. Alignments follow the three-dimensional alignments as defined by available crystal structures. In the alignments, hydrophobic residues are colored black; positive Arg and Lys residues are blue; potentially positive His residues are light blue; negative Asp and Glu residues are red; neutral, polar residues Asn, Gln, Ser, and Thr are green; and Pro residues are brown. Helix S6 may actually begin more N-terminal in the sequence than indicated for some channels of unknown structure (e.g., the Na^+ or Ca^{2+} channels), but the end of S6 is more definite (note the transition from hydrophobic to hydrophilic character). The table is arranged in the following order: ionotropic glutamate receptors; K^+ channels; Na^+ channels; Ca^{2+} channels; and transient receptor potential (TRP) channels. The "Residues" column contains links to the Uniprot sequence, with those particular residues highlighted; the "Uniprot" column contains links to the full Uniprot entry for that channel; and the "PDB" column contains links to a (representative) crystal structure for those channels for which a structure has been determined. Note the extreme conservation of hydrophobic character within the pore cavity, which is highlighted in light yellow. The exceptions to this rule are informative, e.g., the substitution of hydrophobic Ile402 in Kv1.2, which is located at the N terminus (adjacent to the selectivity filter) of the pore cavity, by charged Asp or polar Asn residues in the inwardly rectifying mammalian Kir channels.

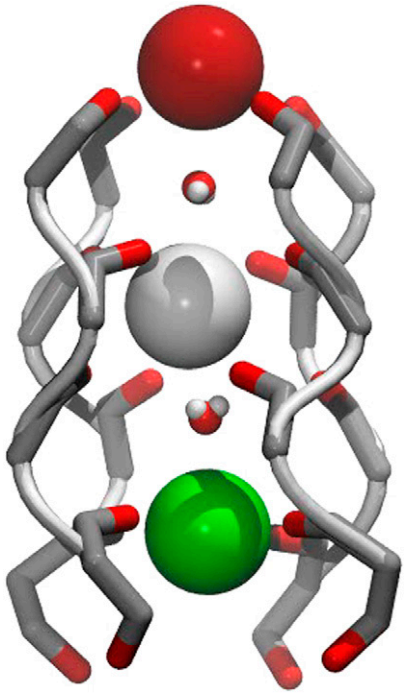

Movie S1. Permeation. K^+ ion (*Large Spheres*) and water molecule (*Red and White*) permeation across the selectivity filter (+123 mV). Kv1.2 residues 374–378 (backbone) and part of the side chain of Thr374 are shown.

Movie S1 (MPG)

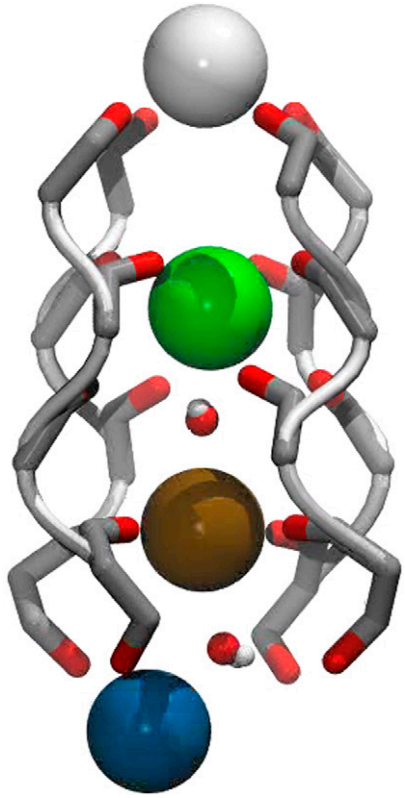

Movie S2. Knock-on mechanism. Excerpt of Supporting Movie S1 at finer frame rate enhancing the detailed motions of K^+ ions and water molecules; a sequence of five consecutive knock-on events by K^+ entering SF site S5 is shown. See also Movie S1 caption.

Movie S2 (MPG)

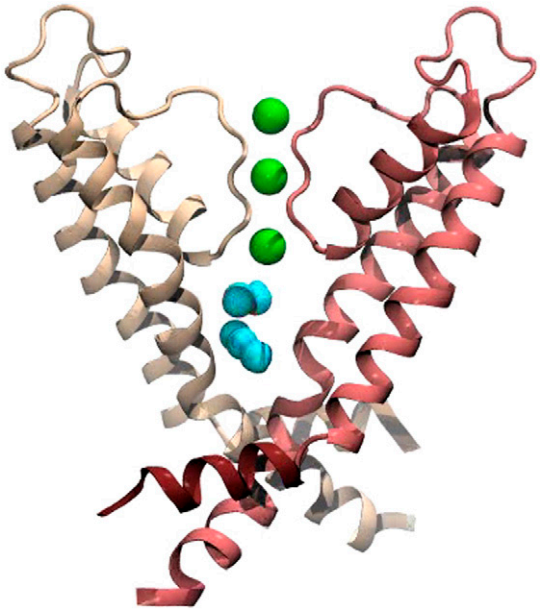

Movie S3. Pore closure: dewetting. Depletion of water molecules (*Blue*) from the pore cavity (−178 mV). Two Kv1.2 subunits are shown, colored as in Fig. 4 (S4–S5 linker helix in darker tones). K^+ ions (*Green Spheres*) within the selectivity filter are also shown.
Movie S3 (MPG)

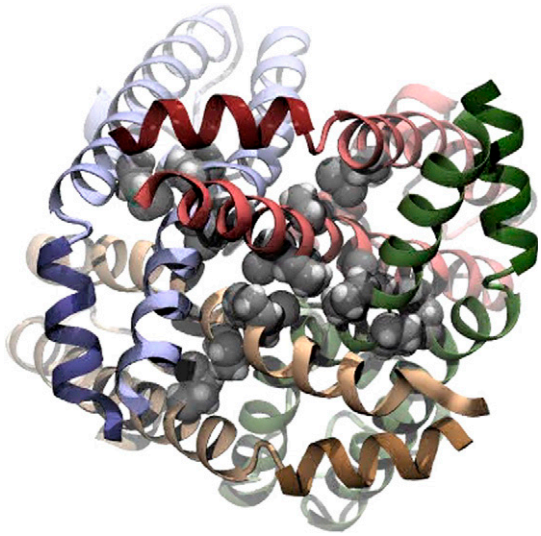

Movie 4. Pore closure: constriction formation. Pore closure viewed from the intracellular side (−178 mV). The four subunits are colored as in Fig. 4, and residues Leu331 and Pro405, Val406, and Pro 407 (PVP constriction) are shown as van der Waals spheres.
Movie S4 (MPG)

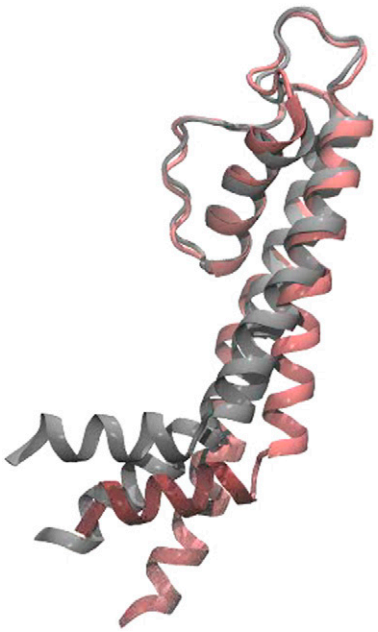

Movie 5. Pore closure: protein conformational changes. Straightening of helix S6 and movement of the S4–S5 linker helix (*Pink*) toward the intracellular side (−178 mV). The X-ray structure (static) is shown in gray. One Kv1.2 subunit is shown.
Movie S5 (MPG)

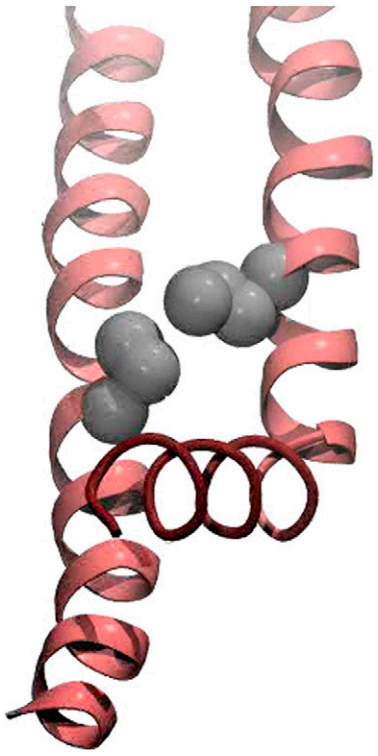

Movie 6. Pore closure: Pro405-Leu331 side chain interchange. Interchange of the side chains of Pro405 (helix S6, *Left*) and Leu 331 (helix S5, *Right*) locks S6 into a straightened conformation (−178 mV). One Kv1.2 subunit is shown.
Movie S6 (MPG)